processes

MDPI

Article

Construction of Fe_2O_3-CuO Heterojunction Photoelectrode for Enhanced Efficiency of Solar Redox Flow Batteries

Ping Lu [1,†], Zihan Zhang [2,†], Zixing Gu [2], Zhuo Li [2], Huaneng Su [2], Xiaozhong Shen [3,*] and Qian Xu [2,3,*]

[1] School of Machinery and Communications, Changzhou Vocational Institute of Industry Technology, Changzhou 213164, China; flightinglp@ciit.edu.cn
[2] Institute for Energy Research, Jiangsu University, Zhenjiang 212013, China; zzh991218@outlook.com (Z.Z.); 2222206025@stmail.ujs.edu.cn (Z.G.); lizhuo19912021@163.com (Z.L.); suhuaneng@ujs.edu.cn (H.S.)
[3] Jiangsu Provincial Engineering Research Center of Key Components for New Energy Vehicle, Wuxi Vocational Institute of Commerce, Wuxi 214153, China
* Correspondence: shenxiaozhong@wxic.edu.cn (X.S.); xuqian@ujs.edu.cn (Q.X.)
† These authors contributed equally to this work.

Abstract: To address the problem of suboptimal performance in deep eutectic solvents displayed by traditional TiO_2 photoelectrodes and Cu_2O photoelectrodes that have undergone simplistic modifications that result in a mismatch with battery discharge capacity, a method combining hydrothermal and dip-coating techniques was developed to create a Fe_2O_3-CuO heterojunction structure on the FTO surface. Then, the impact of the heterojunction structure on the performance of solar flow batteries was investigate in this study. The experimental findings reveal that the formation of the heterojunction structure effectively mitigates the recombination rate of photogenerated carriers within the photoelectrode. Furthermore, by meticulously adjusting the CuO loading, the harmonious balance between charging and discharging currents was achieved, thereby enhancing the overall performance of the solar redox flow batteries. In comparison to standalone Fe_2O_3 photoelectrodes, this innovative approach significantly broadens the spectrum of sunlight utilization. Notably, the fabricated Fe_2O_3/CuO-2 photoelectrode demonstrates a remarkable photocharging performance, far surpassing both Fe_2O_3 photoelectrodes and commercial TiO_2 photoelectrodes. Specifically, the Fe_2O_3/CuO-2 photoelectrode boosts an average current density of 598.68 $\mu A \cdot cm^{-2}$, with its charging current density being 2.74 and 5.15 larger, respectively, than that of the Fe_2O_3 and commercial TiO_2 photoelectrodes.

Keywords: deep eutectic solvent (DES); heterojunction photoelectrode; solar redox flow battery; battery performance

check for updates

Citation: Lu, P.; Zhang, Z.; Gu, Z.; Li, Z.; Su, H.; Shen, X.; Xu, Q. Construction of Fe_2O_3-CuO Heterojunction Photoelectrode for Enhanced Efficiency of Solar Redox Flow Batteries. *Processes* **2024**, *12*, 1765. https://doi.org/10.3390/pr12081765

Academic Editor: Hussein A. Mohammed

Received: 30 July 2024
Revised: 18 August 2024
Accepted: 19 August 2024
Published: 21 August 2024

1. Introduction

A solar redox flow battery (SRFBs) is a system that combines solar cells with a redox flow battery (RFB) by sharing the same electrolyte. Under the irradiation of sunlight, solar energy is absorbed by the photoelectrode in the solar flow battery, and photogenerated electrons and holes are also generated [1]. The photogenerated electrons are transferred to the negative electrolyte through the external circuit for a reduction reaction. The photogenerated holes are transferred into the positive electrolyte through the interface between the photoelectrode and the electrolyte. An oxidation reaction occurs. The transport mode of the electrolyte is similar to that of an RFB. The in situ conversion and storage of solar energy, chemical energy, and electrical energy are realized. The integrated design of the battery has the advantage of reducing the simple energy loss of different devices, has the advantage of being able to cope with energy intermittently and volatility [2]. The electrolyte corrosion of photoelectrodes is an inevitable problem in aqueous SRFBs. At the same time, the application of deep eutectic solvent (DES) in an electrolyte can expand the electrochemical window of the electrolyte. In addition, DES itself does not contain hydrogen ions, which

can inhibit the occurrence of hydrogen evolution reaction from the source and reduce the corrosion effect of the electrolyte on the photoelectrode [3]. The solvent is derived from a mixture of hydrogen bond donors (such as carboxylic acids, amides, alcohols, etc.) and hydrogen bond acceptors (generally ammonium salts) in a certain chemical ratio.

Photoelectrodes have been proven to be effective in expanding the range of sunlight absorption and reducing the recombination rate of photogenerated electrons and holes [4]. In spite of efforts, the heterojunction photoelectrodes fabricated using conventional TiO_2 for SRFBs still exhibit relatively low charging current densities, which fall short of fulfilling the discharge requirements of non-aqueous SRFBs [2]. Within non-aqueous electrolyte systems, the discharge current densities of redox flow batteries and SRFBs typically range around 3–4 $mA \cdot cm^{-2}$. When employing TiO_2 heterojunction photoelectrodes, the disparity between the charging current density and the desired discharge current density lies at approximately an order of magnitude, specifically, of a difference of around tenfold. This implies that, for practical applications, the area of the photoelectrode would need to be more than ten times that of the carbon felt electrode to ensure effective operation. Clearly, such a requirement is impractical in real-world scenarios. As a result, further exploration into modification strategies for photoelectrodes is imperative, with the aim of substantially enhancing the charging current density and narrowing the gap between charging and discharging currents. This endeavor is crucial for laying a solid foundation in terms of performance for subsequent commercialization efforts [5,6].

Metal oxide semiconductors, such as WO_3 [7,8], TiO_2 [9], and ZnO [10], have been utilized as electrode materials for solar cells and solar water splitting with exceptional physical and chemical properties [11,12]. However, the majority of these materials belong to wide-band gap semiconductors that respond only to ultraviolet (UV) or near-UV light. To better harness solar energy, the adoption of electrode materials with a strong visible light response is crucial for enhancing photo absorption and thus generating photogenerated electrons and holes [13,14]. Fe_2O_3, a natural n-type semiconductor material with a narrow bandgap ranging from 1.90 to 2.20 eV, exhibits robust absorption of visible light up to 600 nm, making it a promising candidate in the realm of solar energy devices [15,16]. Pure cubic β-Fe_2O_3 is used as a direct band gap semiconductor. The visible light (<650 nm) is absorbed by the 1.9 eV band gap. Fe_2O_3 is used as a low-cost, non-toxic photofenton reaction catalyst. The degradation of Rhodamine B was studied in detail. Therefore, it is confirmed that hydroxyl radical (OH) is a rather important active substance in this process [15]. Nevertheless, the efficiency of Fe_2O_3 is hampered by the rapid recombination of photogenerated electrons and holes [17]. Firstly, the charge separation efficiency remains substantially hindered by uncontrolled lattice mismatch, leading to severe carrier recombination due to numerous interface trap centers. Therefore, improving lattice matching at interfaces is a highly effective approach to enhancing photovoltaic conversion performance. As we all know, the solar spectrum can be categorized into ultraviolet (UV, 300–400 nm), visible light (Vis, 400–700 nm), and near-infrared (NIR, 700–2500 nm) regions, with UV, Vis, and NIR accounting for 5%, 43%, and 52% of the total solar energy, respectively [18]. Given that the photo absorption of Fe_2O_3 is limited to the UV and Vis regions, coupling Fe_2O_3 with narrow-bandgap semiconductors holds promise in extending its photo absorption range and boosting the charge and discharge performance of solar flow batteries [19].

Currently, researchers have developed many methods to solve this problem. Among them, constructing heterojunctions has been proven to be an effective way to improve the separation of photogenerated electrons and holes [20]. In the past few years, some metal oxide semiconductors, such as NiO, Co_3O_4, and CuO, have been used to construct composites with Fe_2O_3 [21,22]. A novel heterojunction of MoS_2 and α-Fe_2O_3 has been synthesized using the hydrothermal method. The photocatalytic degradation performance of the nano-heterojunction photocatalyst was improved through the increase in the active site of the photocatalyst and the decrease in the photoinduced carrier recombination. The formation of a heterojunction between the two semiconductors leads to the formation of an active photocatalyst. In this system, superoxide radicals, holes, and hydroxyl radi-

cals with potential oxidation were used to obtain an excellent photodegradation effect of organic dyes [23]. ZnO/α-Fe_2O_3 heterojunctions were successfully synthesized using a combination of simple hydrothermal and spin-coating methods [24]. The ZnO/α-Fe_2O_3 heterojunctions not only broadened the visible light absorption but also facilitated the separation and transfer of photogenerated charge carriers, reduced the interfacial resistance between the photoelectrode and electrolyte, and provided a larger electrochemical active surface area compared to pure ZnO nanorods. The hydrothermal approach was utilized to deposit NiCo-LDH cocatalysts onto α-Fe_2O_3 photoanodes [25]. The results indicated that the incorporation of NiCo-LDH significantly enhanced the photocurrent of the α-Fe_2O_3/NiCo-LDH composite photoanode to 0.428 $mA \cdot cm^{-2}$, representing a substantial 4.75-fold increase over the pristine α-Fe_2O_3 electrode. Through mechanism research, it was confirmed that the α-Fe_2O_3/NiCo-LDH heterojunction and NiCo-LDH cocatalyst collectively improved charge separation and transfer within the photoelectrode, thereby facilitating enhanced charge transport properties. Ma et al. conducted research that led to the development of Fe_2O_3/CuO heterojunction photoelectrode films through an immersion technique [26]. These electrodes, when employed in photoelectrochemical water-splitting reactions, exhibited remarkable rates of H_2 and O_2 generation, 0.294 and 0.130 $\mu mol \cdot min^{-1}$, respectively, primarily attributed to their enhanced charge separation efficiency. Nie et al. constructed Cu_2O-based heterostructures with exceptional interfacial charge transfer efficiency, elucidating the mechanisms that enhance their photocatalytic degradation of antibiotics [27]. They also revealed the band structure reconstruction characteristics and photocatalytic reaction pathways, establishing α-Fe_2O_3/Cu_2O heterojunctions via a hydrothermal route. In particular, the p-type Cu-based semiconductor, with its excellent band structure matching, high hole mobility, and good photo absorption capability, is one of the most suitable semiconductors used to form a p-n heterojunction with Fe_2O_3. However, Cu_2O suffers from photo corrosion, resulting in poor stability. At the interface of the heterojunction, the p-type semiconductor region has an internal electric field with negative charges, while the n-type semiconductor region has positive charges. Upon light excitation, photogenerated electrons in the CB of the p-type semiconductor migrate to the CB of the n-type semiconductor within the p-n heterojunction. Concurrently, photogenerated holes in the VB of the n-type semiconductor move to the VB of the p-type semiconductor, driven by the internal electric field. Therefore, the formation of the n-type Fe_2O_3/p-type CuO heterojunction can reduce the recombination of photogenerated electrons and holes, thereby improving the photoelectric conversion efficiency [28,29].

Given the suboptimal performance of photoelectrodes in DES, n-type Fe_2O_3 was combined with p-type CuO to form a novel heterojunction photoelectrode. Subsequently, the photoelectrode was integrated into SRFBs. The formation of this heterojunction structure aims at broadening the solar absorption spectrum of the independent Fe_2O_3 photoelectrode, negatively shifting the flat band potential of the photoelectrode, reducing the recombination rate of photogenerated electrons/holes. These three factors interact with each other to further optimize the photocharging performance in non-aqueous electrolyte. This advancement presents a viable option for the eventual commercialization of solar redox flow battery–electrofuel systems.

2. Materials and Methods

2.1. Preparation of Fe_2O_3-CuO Heterojunction Photoelectrode

The preparation process of a Fe_2O_3-CuO heterojunction photoelectrode is shown in Figure 1.

The preparation of the Fe_2O_3-CuO heterojunction photoelectrode is conducted in two consecutive steps:

(1) Growth of Fe_2O_3 on Fluorine-Doped Tin Oxide (FTO) via Hydrothermal Method: Initially, the FTO substrate is thoroughly cleaned with deionized water and absolute ethanol, followed by drying at 50 °C. Then, a precursor solution is prepared by mixing 0.15 M $FeCl_3$ and 1 M $NaNO_3$. This precursor solution, along with the cleaned FTO, is placed in a

polytetrafluoroethylene-lined autoclave and heated to 100 °C for a reaction period of 10 h. After the reaction, the FTO is rinsed thoroughly with deionized water and subsequently annealed at 650 °C for 2 h to obtain the Fe_2O_3 electrode.

(2) Fabrication of Fe_2O_3-CuO Electrode through Dip-Coating Method: Firstly, a small quantity of polyethylene glycol and nano-sized copper oxide particles with diameters ranging from 50 to 100 nm are dispersed in absolute ethanol, and the solution is subjected to ultrasonic treatment to ensure a uniform dispersion. The prepared Fe_2O_3 electrode is then dipped into this solution for 3 min each time, with the dipping process repeated 1, 2, or 3 times as desired. The rotational speed used was 5000 r/min, and the time was 60 s. The electrodes were uniformly rotated 1, 2, and 3 times by a spin coater (EZ4-S-PP). After each completion, it was dried in a drying oven at 60 °C. Finally, the electrode was annealed at 450 °C to yield the Fe_2O_3-CuO heterojunction electrode.

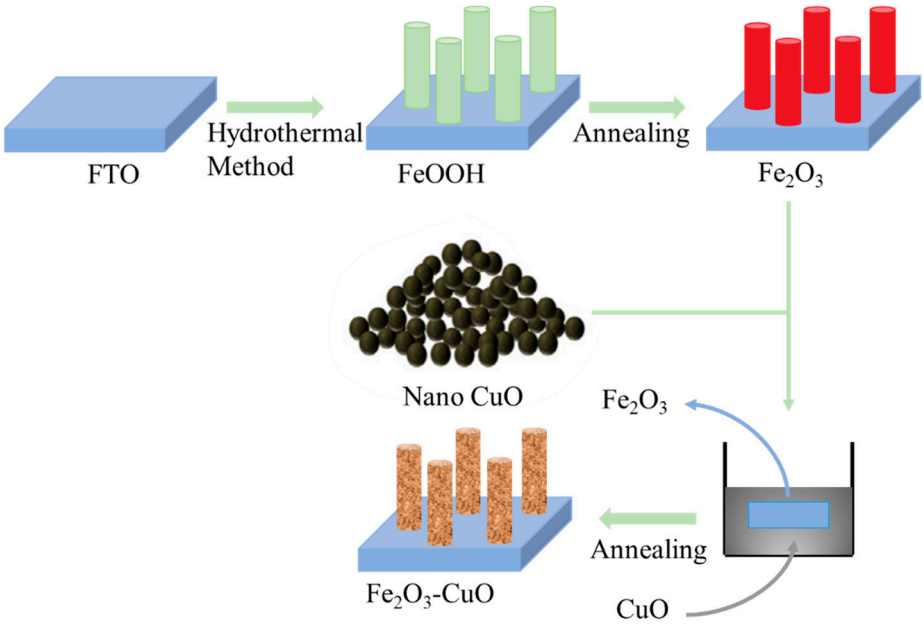

Figure 1. Flow chart for the preparation of Fe_2O_3-CuO heterojunction photoelectrode.

It is essential to store the prepared photoelectrode in a light-shielded and airtight container to prevent any degradation or contamination.

2.2. Preparation of DES and Electrolyte

The DES, commonly known as "ethaline" was prepared by mixing choline chloride ($C_5H_{14}ClNO$, 98%, Aladdin, Shanghai, China) and ethylene glycol ($(CH_2OH)_2$, 99%, Sinopharm Reagent, Shanghai, China) in a molar ratio of 1:2. A certain amount of TEMPO ($C_9H_{18}NO$, 98%, Macklin, Shanghai, China) and VCl_3 (97%, Aladdin, Shanghai, China) were put into the DES mentioned above to form an electrolyte with a certain concentration.

2.3. Electrochemical and Photoelectrochemical Test

Electrochemical workstations (CHI604 in Shanghai, China and Ivium in Eindhoven, The Netherlands) were used to test the performance of the electrolyte/photoanode interface. A three-electrode system was used during the test. A 1 cm^2 FTO/ Fe_2O_3-CuO photoanode (in SRFB half-cell test mode) was immersed in the electrolyte as the working electrode, with a platinum electrode as the counter electrode and a saturated calomel electrode as the reference electrode. In solar flow battery half-cell mode, linear voltammetry and the Mott–Schottky curve test were used. Different electrolytes' physical properties and electrochemical characteristics were tested under the selected electrode.

The photoanode was embedded in the collector plate, and the graphite felt was placed on the anode collector plate. The photoanode and the graphite felt electrode on the anode

side were dislocated. The Nafion212 film, cathode side graphite felt, cathode collector plate, and plexiglass were sequenced. Then, it was fixed through four studs to form the SRFB. Photocharging curves were carried out on the device.

3. Results

3.1. Photoelectrochemical Performance

The photoelectrodes immersed one, two, and three times were named Fe_2O_3/CuO-1, Fe_2O_3/CuO-2, and Fe_2O_3/CuO-3, respectively. Four types of electrodes were placed in an electrolyte composed of 0.10 mol·L^{-1} TEMPO and low eutectic solvent for electrochemical testing. The linear voltammetry scanning results are shown in Figure 2.

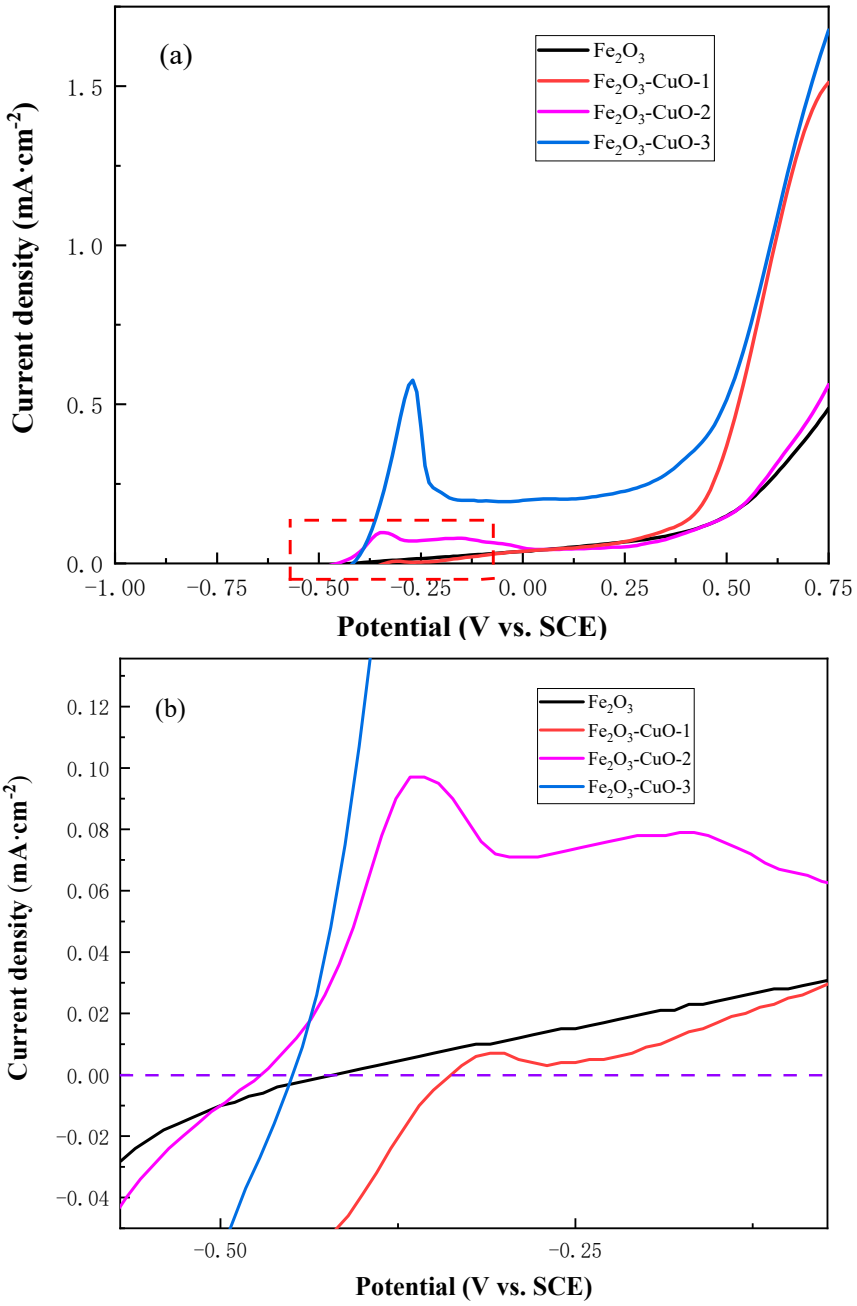

Figure 2. Linear scanning (LSV) test results of Fe_2O_3 photoelectrode, Fe_2O_3/CuO-1 photoelectrode, Fe_2O_3/CuO-2 photoelectrode, and Fe_2O_3/CuO-3 photoelectrode.

Under sufficient sunlight irradiation, the photoelectrode itself will generate a photovoltage due to the generation of photogenerated carriers. In LSV testing, the electrochemical workstation applies a certain voltage on the electrode surface, and the voltage changes from low potential to high potential at a certain rate. At this time, during the scanning process, there will be zero current density at non-zero potential points in dashed lines due to the cancelation of the photovoltage. Therefore, relevant information on the photoelectric aurora voltage can be obtained from the LSV curve. Figure 2b is a magnification of the curve within the red box in Figure 2a. In Figure 2b, it can be seen that with the increase in immersion times, the electrode current density returns to zero and gradually moves toward the negative potential direction. This indicates that the addition of CuO can give the electrode a higher photovoltage (0.47 V), thus providing higher performance for the battery. However, when the immersion frequency reaches three times, excessive CuO will actually reduce its photovoltage. It can be inferred that the increase in layer thickness increases the diffusion distance of photogenerated carriers, which can be recombined without being transferred to the electrolyte for redox reaction. Therefore, the optimal number of immersion times is two, and the total immersion time is 6 min.

In drawing tangents along the straight lines of the four curves, their points of intersection with the X-axis can be obtained. It can be seen that the M-S curve slopes in Figure 3 of all four electrodes are positive, indicating that they are all n-type semiconductors.

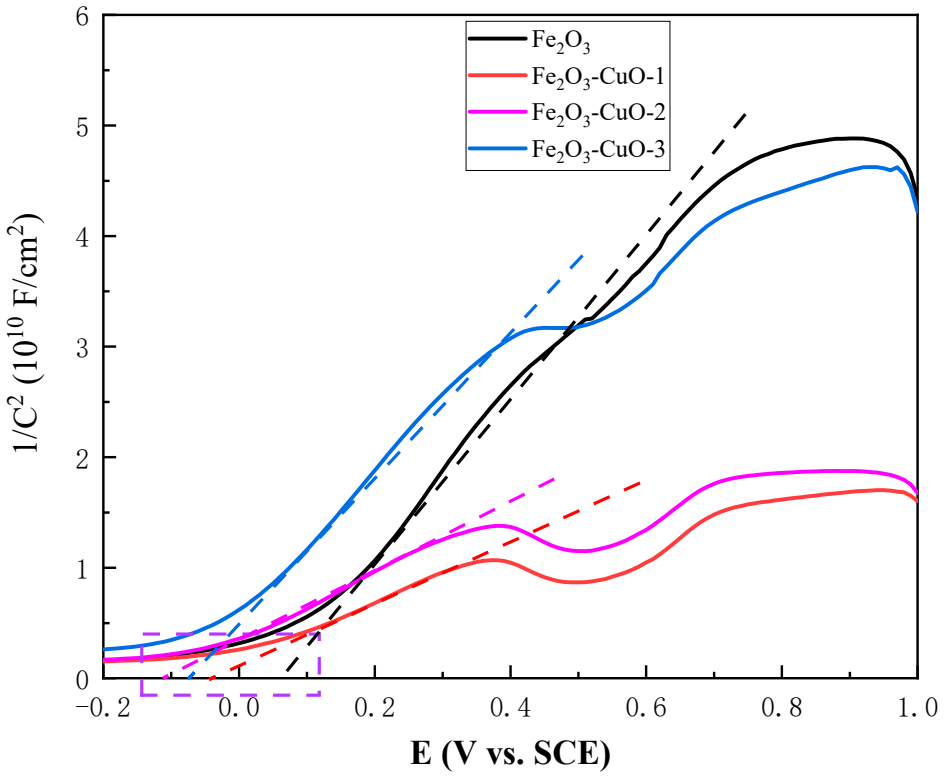

Figure 3. Mott–Schottky test results for Fe_2O_3 photoelectrode, Fe_2O_3/CuO-1 photoelectrode, Fe_2O_3/CuO-2 photoelectrode, and Fe_2O_3/CuO-3 photoelectrode.

Therefore, with the addition of p-type semiconductor CuO, p-n heterojunctions can be formed to improve electrode performance. The results show that the flat band potentials of the Fe_2O_3 photoelectrode, Fe_2O_3/CuO-1 photoelectrode, Fe_2O_3/CuO-2 photoelectrode, and Fe_2O_3/CuO-3 photoelectrode were 0.07, −0.05, −0.12, and −0.081 V vs. SCE, respectively. With the addition of CuO, the flat band potential of the electrode gradually shifts toward a negative potential and reaches its extreme value when the number of immersion cycles is two. The negative shift of the flat band potential allows the photoelectrode to provide a higher photovoltage, which can provide higher performance to the battery.

Meanwhile, the carrier concentration of the Fe_2O_3/CuO-2 photoelectrode is higher than that of the pure Fe_2O_3 photoelectrode according to the slope of the dashed line fitted on the M-S curve. The transport and reaction rate of photogenerated carriers is one of the key factors affecting the photoelectric performance. A high carrier concentration indicates high photogenerated carrier generation and transport rate, which means that the formation of a Fe_2O_3/CuO heterojunction can restrain the recombination of photogenerated electrons and holes. In addition, the thickness of the diffusion layer also affects the transport of photogenerated carriers. When the number of impregnations is two, the thick diffusion layer can avoid the occurrence of photogenerated carrier recombination before reaction in solution.

3.2. Physical Properties of Fe_2O_3-CuO Heterojunction Photoelectrode

The XRD test results of four electrodes are shown in Figure 4, which can be used to analyze the crystal structure of the photoelectrode.

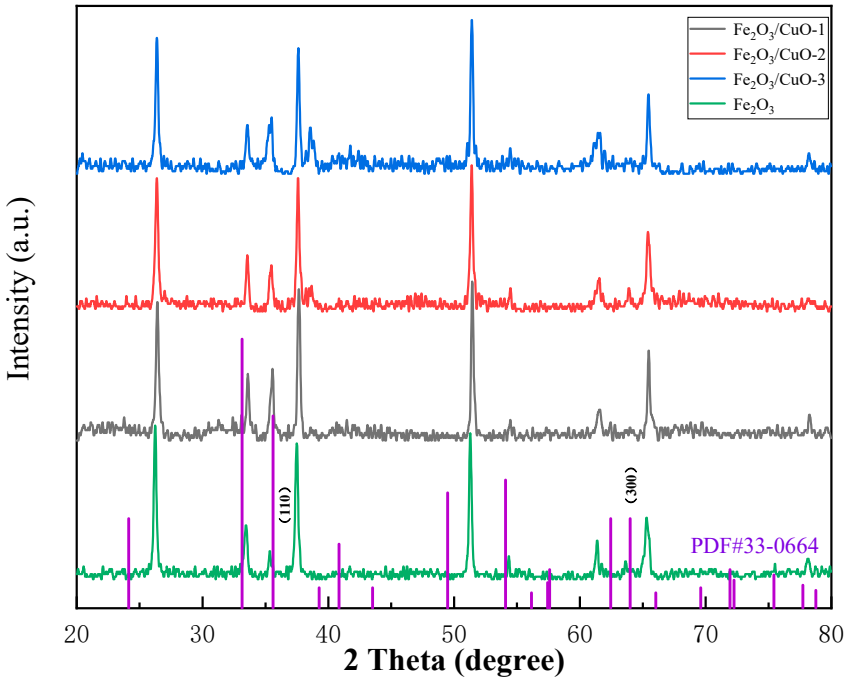

Figure 4. X-ray diffractograms of Fe_2O_3 photoelectrode, Fe_2O_3/CuO-1 photoelectrode, Fe_2O_3/CuO-2 photoelectrode, and Fe_2O_3/CuO-3 photoelectrode.

The diffraction peaks of the Fe_2O_3 photoelectrode at 35.60° and 64° can be well matched with the (110) and (300) crystal planes of hematite phase Fe_2O_3 (PDF # 33-0664). Since the electrode substrate is FTO, the diffraction peaks at 26.61°, 37.92°, 51.79°, 61.91°, and 65.91° are the (110), (200), (210), (310), and (301) crystal planes of SnO_2. After adding CuO to the Fe_2O_3 photoelectrode, new diffraction peaks appeared on the electrode surface at positions 35.46° and 38.54°. These two diffraction peaks correspond to the (002) and (111) crystal planes of CuO, respectively. Meanwhile, with the increase in immersion times, two diffraction intensities gradually increase. This indicates that as the number of immersion cycles increases, the CuO content on the surface of the photoelectrode also gradually increases. However, the specific content and distribution of CuO need to be further confirmed using XPS and SEM characterization techniques [30].

In order to further detect the material composition on the electrode surface, XPS testing was conducted on the sample, and the best performing Fe_2O_3/CuO-2 photoelectrode and Fe_2O_3 photoelectrode were selected as the test electrodes. The XPS test results of two electrodes are shown in Figure 5. The binding energy of 284.80 eV for the C 1s peak was used to calibrate the test results [31]. Figure 5a shows the full spectrum of the XPS of

the two electrodes. From the full spectrum data of the Fe_2O_3/CuO-2 photoelectrode, it can be seen that a new peak appears in the dashed lines range of 900–960 eV, which proves the addition of the Cu element and the successful growth of CuO on Fe_2O_3.

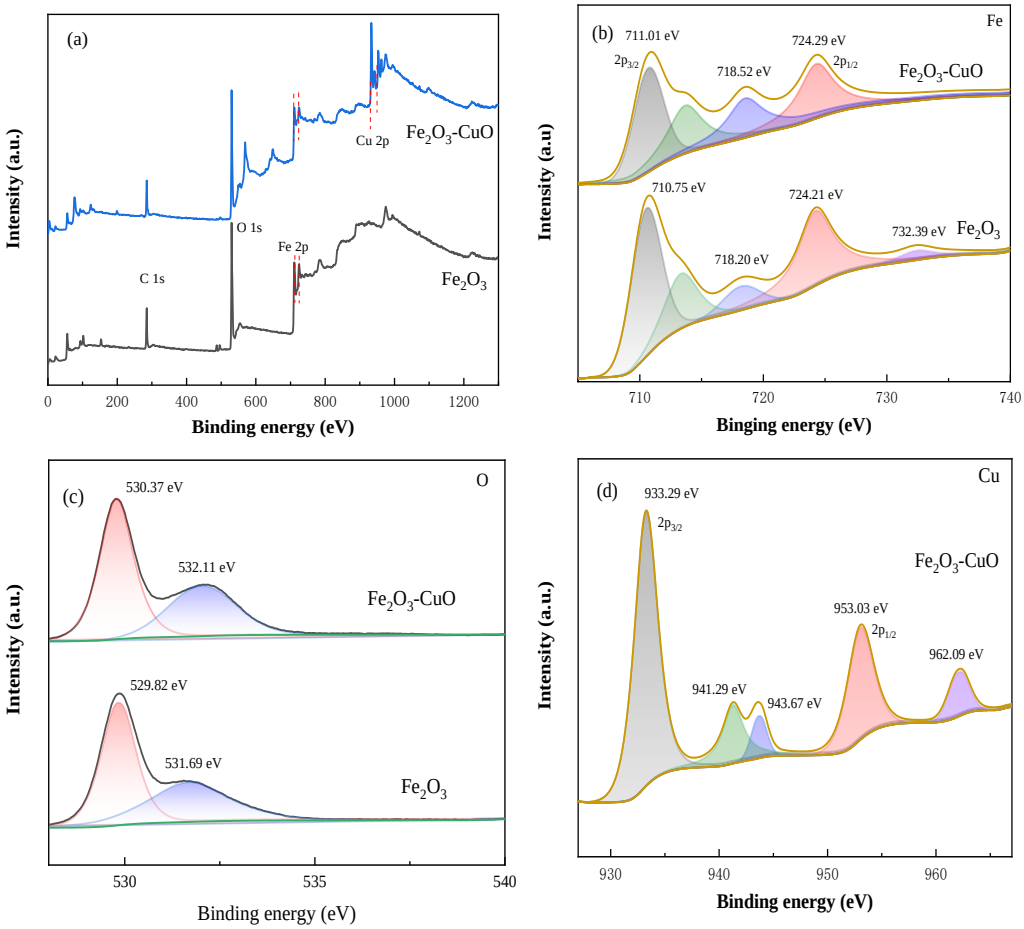

Figure 5. XPS test results for Fe_2O_3 photoelectrode, Fe_2O_3/CuO-2 photoelectrode: (**a**) full spectrum; (**b**) Fe 2p; (**c**) O 1s; (**d**) Cu 2p.

Through analyzing the Fe 2p spectra of two electrodes (Figure 5b), the typical binding energies of Fe_2O_3 can be clearly observed around 710.75 eV and 724.21 eV, using Fe $2p_{3/2}$ and Fe $2p_{1/2}$, respectively. In contrast, the Fe 2p peak of the Fe_2O_3/CuO-2 photoelectrode moves toward higher binding energy, which indicates the strong interaction between N-type Fe_2O_3 and CuO.

For the O 1s spectra of these two electrodes (Figure 5c), the peak at 529.82 eV is attributed to the Fe-O bond, while the peak at 532.11 eV is attributed to the combined effect of Cu-O and Fe-O bonds.

For the Fe_2O_3/CuO-2 photoelectrode, the Cu 2p test results are shown in Figure 5d, with a total of five peaks. The peaks at 933.29 eV and 953.08 eV are Cu $2p_{3/2}$ and Cu $2p_{1/2}$, respectively. The distance between these two peaks is 19.79 eV, indicating that the Cu^{2+} in the Fe_2O_3/CuO-2 photoelectrode is similar to the peak prepared by similar work. The peaks at 941.29 eV and 962.09 eV are oscillatory satellite peaks of Cu^{2+} [32].

Figure 6 shows the UV-vis spectrum test results of four kinds of photoelectrodes. It can be seen from the figure that the absorption limit of the pure Fe_2O_3 photoelectrode is about 600 nm. With the addition of CuO, the Fe_2O_3/CuO electrode has a tendency to expand to 800 nm, which gradually approaches the absorption limit of pure CuO (800 nm). At the same time, with the addition of CuO, the absorption capacity of the photoelectrode is gradually enhanced in the ultraviolet spectrum in the range of 200–400 nm. However, when the number of impregnations reaches three, due to the excessive addition of CuO,

the absorption capacity of the electrode is significantly reduced and ultimately lower than the absorption capacity of the pure Fe_2O_3 photoelectrode.

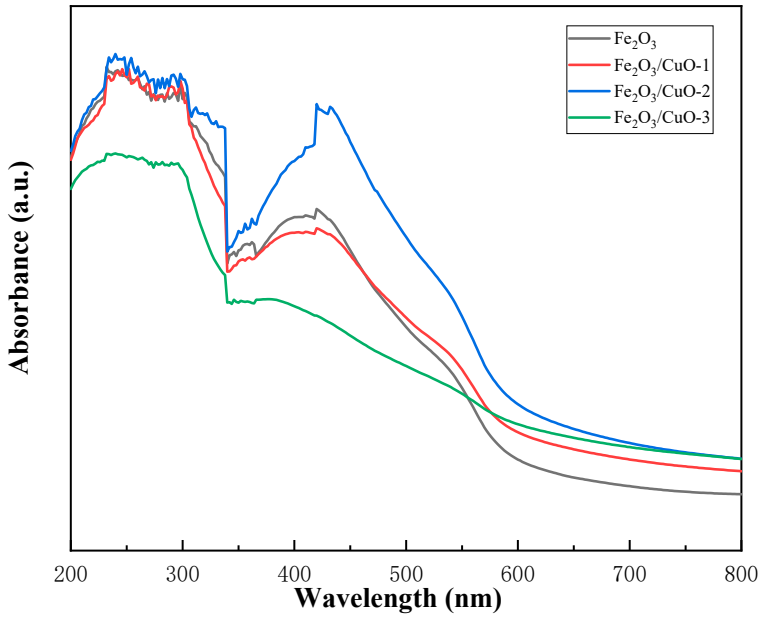

Figure 6. UV-visible spectra of Fe_2O_3 photoelectrode, Fe_2O_3/CuO-1 photoelectrode, Fe_2O_3/CuO-2 photoelectrode, and Fe_2O_3/CuO-3 photoelectrode.

The morphology of the Fe_2O_3 photoelectrode, Fe_2O_3/CuO-1 photoelectrode, and Fe_2O_3/CuO-3 photoelectrode was characterized using SEM, as shown in Figure 7.

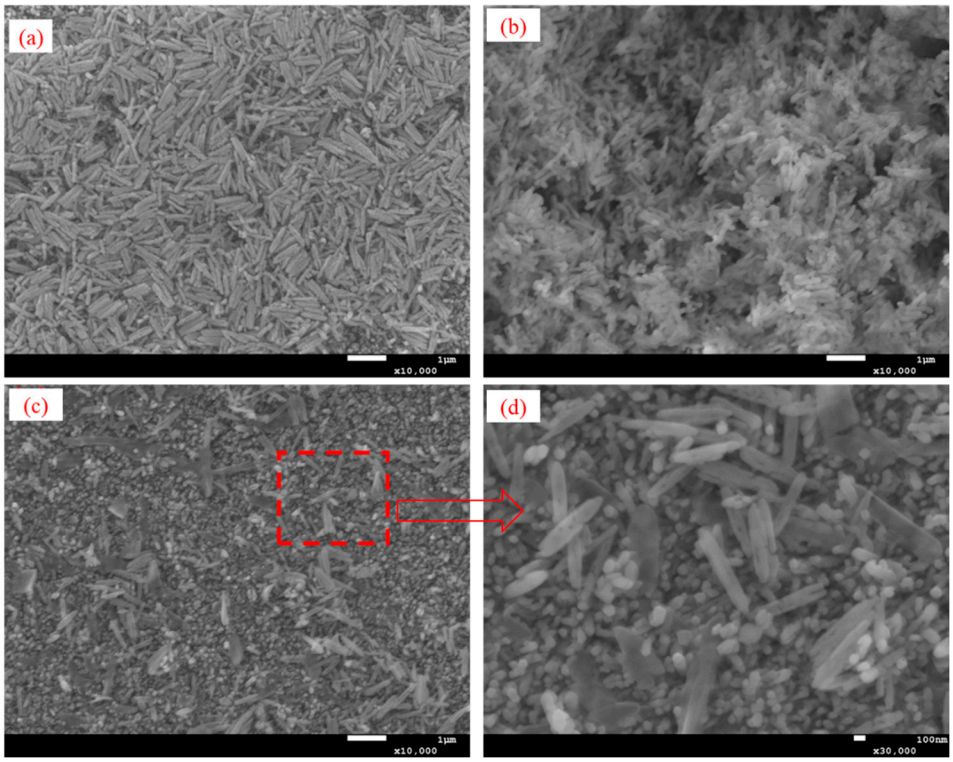

Figure 7. SEM images of (**a**) Fe_2O_3 photoelectrode; (**b**) Fe_2O_3/CuO-1 photoelectrode; (**c**) Fe_2O_3/CuO-3 photoelectrode; and (**d**) Fe_2O_3/CuO-3 photoelectrode (high magnification).

As shown in Figure 7a, Fe_2O_3 nanorods loaded on FTO have a relatively smooth surface and no secondary structure. However, as observed in Figure 7b,c, for the Fe_2O_3/Cuo-1 photoelectrode and Fe_2O_3/CuO-3 photoelectrode, the CuO nanoparticles adhere closely to the surface of the Fe_2O_3 nanorods after the impregnation [26]. This can be clearly seen in the high-resolution SEM image of the Fe_2O_3/CuO-3 photoelectrode (Figure 7d).

Figure 8 shows the distribution of elements and content of each element on the surface of Fe_2O_3/CuO-3 photoelectrode.

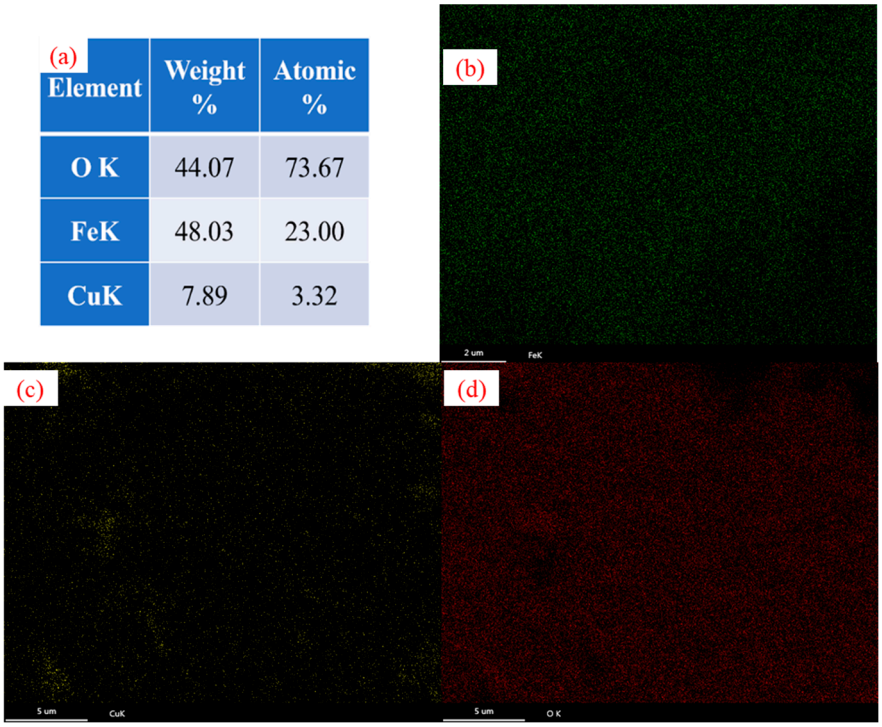

Element	Weight %	Atomic %
O K	44.07	73.67
FeK	48.03	23.00
CuK	7.89	3.32

Figure 8. EDS spectra and elemental distribution of Fe_2O_3/CuO-3 photoelectrodes: (**a**) Elemental content; (**b**) Fe; (**c**) Cu; (**d**) O.

The molar mass ratio of CuO to Fe_2O_3 in the Fe_2O_3/CuO-3 photoelectrode is 0.15:1, according to the element mass percentage in Figure 8a. The distribution of elements on the surface of the photoelectrode was obtained using an EDS element atlas. Fe and O grow uniformly on the surface of the photoelectrode, but the content of Cu element in the box part of Figure 8c is small, and there is a certain imbalance of CuO on the surface, which may be the reason for the deterioration of the performance after the third dip in the LSV.

3.3. Performance of Fe_2O_3-CuO Heterojunction Photoelectrode on SRFBs Using DES Electrolyte

The excellent performance of the Fe_2O_3/CuO-2 photoelectrode was confirmed by the half-cell test of the two photoelectrodes. The photocharging performance of the Fe_2O_3/CuO-2 photoelectrode was tested under standard sunlight using an electrochemical workstation. The test results are shown in Figure 9.

The long-term operating temperature of the simulated SRFBs was controlled at 35 °C. At the same time, TEMPO was used as a redox substance on one side of the photoelectrode, and V^{2+}-V^{3+} was used as a redox substance on the other side. The experimental results show that the average current density of Fe_2O_3/CuO-2 photoelectrode can reach 598.68 $\mu A \cdot cm^{-2}$, while that of Fe_2O_3 photoelectrode is only 218.34 $\mu A \cdot cm^{-2}$ under the condition of 30 min of photocharging. Electrochemical tests show that the photocharging performance of the SRFBs is significantly improved, and the charging current does not attenuate significantly during the longer charging process. This is consistent with the test results of the M-S curve. In other words, under the condition of solar energy, the carrier concentration of the

Fe_2O_3/CuO-2 photoelectrode is higher than that of Fe_2O_3 photoelectrode, which is due to the formation of the Fe_2O_3/CuO heterojunction.

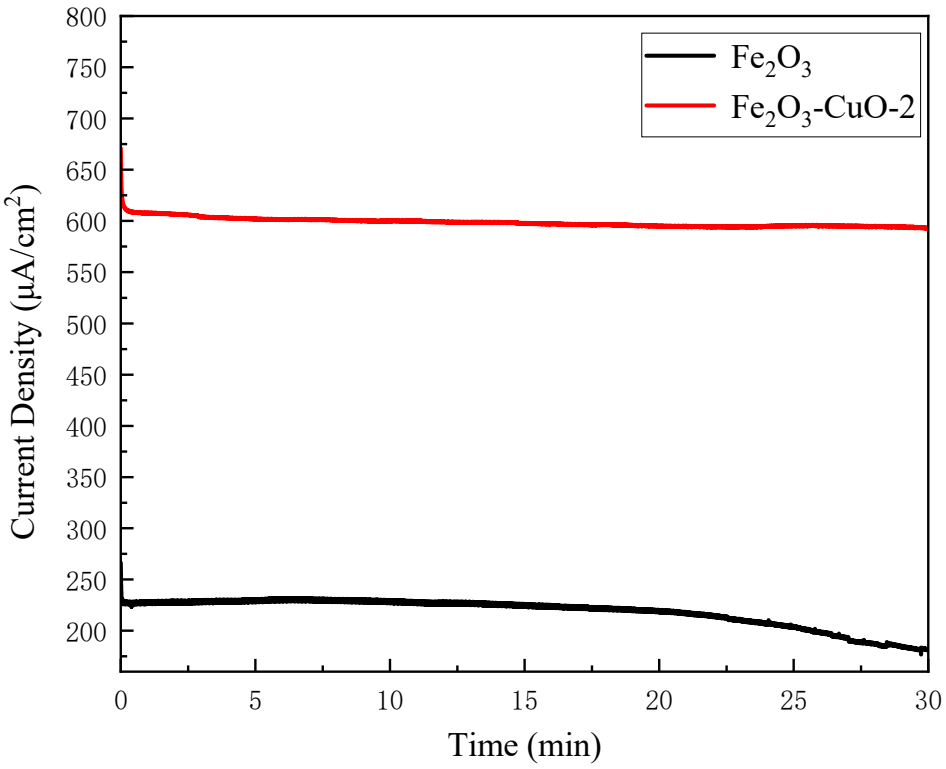

Figure 9. Unbiased photocharging curves of Fe_2O_3 photoelectrode and Fe_2O_3/CuO-2 photoelectrode.

4. Conclusions

Given the suboptimal performance of photoelectrodes in DES, the combined approach was devised utilizing hydrothermal and dip-coating techniques to synthesize Fe_2O_3-CuO heterojunction structures directly on the surface of FTO. By carefully modulating the CuO loading, the absorption spectrum was successfully broadened, extending from the ultraviolet into the visible light range. Moreover, the formation of the heterojunction structure effectively shifts the flat band potential of the photoelectrode toward a more negative value, aiding in the suppression of photogenerated carrier recombination rates. This enhancement holds significant promise for improving the performance of SRFBs as follows:

(1) In comparison to standalone Fe_2O_3 photoelectrodes, the fabricated Fe_2O_3/CuO-2 photoelectrode exhibits remarkable photocharging capabilities, surpassing both Fe_2O_3 and commercial TiO_2 photoelectrodes by a wide margin.
(2) Notably, the Fe_2O_3/CuO-2 photoelectrode boasts an average current density of 598.68 $\mu A \cdot cm^{-2}$, significantly higher than the 218.34 $\mu A \cdot cm^{-2}$ of the Fe_2O_3 photoelectrode and the 116.21 $\mu A \cdot cm^{-2}$ of the TiO_2 photoelectrode.
(3) Specifically, its charging current density is 2.74 times and 5.15 times that of the Fe_2O_3 and TiO_2 photoelectrodes, respectively.

Author Contributions: Writing—original draft and writing—review and editing, P.L.; validation and writing—original draft, Z.Z.; methodology, Z.G.; investigation, Z.L.; writing—review and editing, H.S.; funding acquisition, writing—review and editing, X.S.; funding acquisition and writing—review and editing, Q.X. All authors have read and agreed to the published version of the manuscript.

Funding: The work described in this paper was fully supported by grants from Jiangsu Natural Science Foundation (No. BK20231323), State Key Laboratory of Engine at Tianjin University (No. K2020-14), High-Tech Research Key Laboratory of Zhenjiang City (No. SS2018002), and a Project

Funded by the Priority Academic Program Development of Jiangsu Higher Education Institutions (PAPD), China.

Data Availability Statement: Data are contained within this article.

Conflicts of Interest: The authors declare no conflict of interest.

References

1. Yu, M.; McCulloch, W.D.; Beauchamp, D.R.; Huang, Z.; Ren, X.; Wu, Y. Aqueous lithium–iodine solar flow battery for the simultaneous conversion and storage of solar energy. *J. Am. Chem. Soc.* **2015**, *137*, 8332–8335.
2. Lu, P.; Sun, P.; Ma, Q.; Su, H.; Leung, P.; Yang, W.; Xu, Q. Rationally Designed Ternary Deep Eutectic Solvent Enabling Higher Performance for Non-Aqueous Redox Flow Batteries. *Processes* **2022**, *10*, 649. [CrossRef]
3. Miao, J.; Yang, Y.; Cui, P.; Ru, C.; Zhang, K. Improving Charge Transfer Beyond Conventional Heterojunction Photoelectrodes: Fundamentals, Strategies and Applications. *Adv. Funct. Mater.* **2024**, 2406443. [CrossRef]
4. Lu, P.; Gu, Z.; Zhang, Z.; Su, H.; Ma, Q.; Li, C.; Wei, L.; Xu, Q. Outside-to-inside: Efficacy comparation of Mn bulk and surface-doped TiO_2{201} in E-fueled solar flow battery system. *Surf. Interfaces* **2024**, *46*, 104174.
5. Kim, Y.; Seo, J.-W.; Lee, I.-H.; Kim, J.-Y. Investigating the Influence of PbS Quantum Dot-Decorated TiO_2 Photoanode Thickness on Photoelectrochemical Hydrogen Production Performance. *Materials* **2024**, *17*, 225.
6. Wakatsuki, N.; Tojo, T. Fabrication of Titanium Oxide Thin-Film Electrodes with Photocatalytic Activities and an Evaluation of Their Photoelectrochemical Properties. *Eng. Proc.* **2023**, *55*, 57. [CrossRef]
7. Costa, M.B.; de Araújo, M.A.; Tinoco, M.V.d.L.; Brito, J.F.d.; Mascaro, L.H. Current trending and beyond for solar-driven water splitting reaction on WO_3 photoanodes. *J. Energy Chem.* **2022**, *73*, 88–113.
8. Momin, R.B.N.; Rajput, R.B.; Shaikh, R.S.; Kale, R.B. A review of WO_3-based dye-sensitized solar cells: Unveiling the potential of tungsten oxide as counter and working electrodes. *Mater. Sci. Semicond. Process.* **2024**, *181*, 108662.
9. Mohd Amin, N.A.A.; Mohd Zaid, H.F. A review of hydrogen production using TIO_2-based photocatalyst in tandem solar cell. *Int. J. Hydrogen Energy* **2024**, *77*, 166–183.
10. Jiang, Z.; Cheng, B.; Zhang, L.; Zhang, Z.; Bie, C. A review on ZnO-based S-scheme heterojunction photocatalysts. *Chin. J. Catal.* **2023**, *52*, 32–49.
11. Maragno, A.R.A.; Morozan, A.; Fize, J.; Pellat, M.; Artero, V.; Charton, S.; Matheron, M. Thermally integrated photoelectrochemical devices with perovskite/silicon tandem solar cells: A modular approach for scalable direct water splitting. *Sustain. Energy Fuels* **2024**, *8*, 3726–3739.
12. Kumar, S.G.; Rao, K.S.R.K. Comparison of modification strategies towards enhanced charge carrier separation and photocatalytic degradation activity of metal oxide semiconductors (TiO_2, WO_3 and ZnO). *Appl. Surf. Sci.* **2017**, *391*, 124–148.
13. Zhang, J.-X.; Zhao, Z.-Y.; Yang, T.-L.; Yang, J.; Zhang, J.; Liu, Q.-J.; Kuang, Y. Harnessing intrinsic defect complexes for visible-light-driven photocatalytic activity in Delafossite $CuAlO_2$. *Acta Mater.* **2024**, *269*, 119801.
14. Ryabchuk, V. Photophysical processes related to photoadsorption and photocatalysis on wide band gap solids: A review. *Int. J. Photoenergy* **2004**, *6*, 582750.
15. Zhang, Y.; Zhang, N.; Wang, T.; Huang, H.; Chen, Y.; Li, Z.; Zou, Z. Heterogeneous degradation of organic contaminants in the photo-Fenton reaction employing pure cubic β-Fe_2O_3. *Appl. Catal. B Environ.* **2019**, *245*, 410–419.
16. Li, J.; You, J.; Wang, Z.; Zhao, Y.; Xu, J.; Li, X.; Zhang, H. Application of α-Fe_2O_3-based heterogeneous photo-Fenton catalyst in wastewater treatment: A review of recent advances. *J. Environ. Chem. Eng.* **2022**, *10*, 108329.
17. Liang, S.; Zheng, L.-J.; Song, L.-N.; Wang, X.-X.; Tu, W.-B.; Xu, J.-J. Accelerated Confined Mass Transfer of MoS_2 1D Nanotube in Photo-Assisted Metal–Air Batteries. *Adv. Mater.* **2024**, *36*, 2307790.
18. Fontenla, J.; White, O.R.; Fox, P.A.; Avrett, E.H.; Kurucz, R.L. Calculation of solar irradiances. I. Synthesis of the solar spectrum. *Astrophys. J.* **1999**, *518*, 480.
19. Liao, A.; He, H.; Zhou, Y.; Zou, Z. Typical strategies to facilitate charge transfer for enhanced oxygen evolution reaction: Case studies on hematite. *J. Semicond.* **2020**, *41*, 091709.
20. Li, W.; Li, J.-J.; Liu, Z.-F.; Ma, H.-Y.; Fang, P.-F.; Xiong, R.; Wei, J.-H. Fast charge transfer kinetics in Sv-$ZnIn_2S_4$/Sb_2S_3 S-scheme heterojunction photocatalyst for enhanced photocatalytic hydrogen evolution. *Rare Met.* **2024**, *43*, 533–542.
21. Huang, W.; Zhang, D.; Wang, M. A Review: Research Progress on Photoelectric Catalytic Water Splitting of α-Fe_2O_3. *Curr. Nanosci.* **2023**, *19*, 758–769.
22. Shaheen, S.; Li, Z.; Zada, A.; Bian, J.; Zhang, Z.; Qu, Y.; Jing, L. Recent advances in modulating charge separation of α-Fe_2O_3-based photocatalysts. *Surf. Interfaces* **2024**, *44*, 103623.
23. Chen, L.; Arshad, M.; Chuang, Y.; Nguyen, T.-B.; Wu, C.-H.; Chen, C.-W.; Dong, C.-D. A novel nano-heterojunction MoS_2/α-Fe_2O_3 photocatalysts with high photocatalytic and photoelectrochemical performance under visible light irradiation. *J. Alloys Compd.* **2023**, *947*, 169577.
24. Zhang, R.; Zhao, G.; Hu, J.; Lu, P.; Liu, S.; Li, X. Enhanced photoelectrochemical performance of ZnO/α-Fe_2O_3 heterojunction photoelectrode fabricated by facile hydrothermal and spin-coating method. *Int. J. Hydrogen Energy* **2024**, *51*, 633–642.
25. Zhang, B.; Ruan, M.; Wang, C.; Guo, Z.; Liu, Z. Enhanced photoelectrochemical performance of α-Fe_2O_3 photoanode modified with NiCo layered double hydroxide. *J. Electroanal. Chem.* **2023**, *936*, 117388.

26. Ma, J.; Wang, Q.; Li, L.; Zong, X.; Sun, H.; Tao, R.; Fan, X. Fe_2O_3 nanorods/CuO nanoparticles p-n heterojunction photoanode: Effective charge separation and enhanced photoelectrochemical properties. *J. Colloid Interface Sci.* **2021**, *602*, 32–42.
27. Nie, J.; Yu, X.; Wei, Y.; Liu, Z.; Zhang, J.; Yu, Z.; Ma, Y.; Yao, B. Interfacial charge transfer effects of α-Fe_2O_3/Cu_2O heterojunction and enhancement mechanism of its photocatalytic oxidation. *Process Saf. Environ. Prot.* **2023**, *170*, 241–258.
28. Yang, H. A short review on heterojunction photocatalysts: Carrier transfer behavior and photocatalytic mechanisms. *Mater. Res. Bull.* **2021**, *142*, 111406.
29. Wang, D.; Liu, X.; Kang, Y.; Wang, X.; Wu, Y.; Fang, S.; Yu, H.; Memon, M.H.; Zhang, H.; Hu, W.; et al. Bidirectional photocurrent in p–n heterojunction nanowires. *Nat. Electron.* **2021**, *4*, 645–652.
30. Saleem, M.H.; Ejaz, U.; Vithanage, M.; Bolan, N.; Siddique, K.H.M. Synthesis, characterization, and advanced sustainable applications of copper oxide nanoparticles: A review. *Clean Technol. Environ. Policy* **2024**. [CrossRef]
31. Pastrana, E.C.; Zamora, V.; Wang, D.; Alarcón, H. Fabrication and characterization of α-Fe_2O_3/CuO heterostructure thin films via dip-coating technique for improved photoelectrochemical performance. *Adv. Nat. Sci. Nanosci. Nanotechnol.* **2019**, *10*, 035012.
32. Gao, Y.; Zhang, N.; Wang, C.; Zhao, F.; Yu, Y. Construction of Fe_2O_3@CuO Heterojunction Nanotubes for Enhanced Oxygen Evolution Reaction. *ACS Appl. Energy Mater.* **2020**, *3*, 666–674.